RESEARCH ARTICLE

WILEY

Artificial visual-tactile perception array for enhanced memory and neuromorphic computations

Jiaqi He[1,2] | **Ruilai Wei**[1] | **Shuaipeng Ge**[1] | **Wenqiang Wu**[3] | **Jianchao Guo**[1,2] | **Juan Tao**[1] | **Ru Wang**[1,3] | **Chunfeng Wang**[1,3] | **Caofeng Pan**[1,2] ⓘ

[1]CAS Center for Excellence in Nanoscience, Beijing Key Laboratory of Micro-nano Energy and Sensor, Beijing Institute of Nanoenergy and Nanosystems, Chinese Academy of Sciences, Beijing, the People's Republic of China

[2]School of Nanoscience and Engineering, University of Chinese Academy of Sciences, Beijing, the People's Republic of China

[3]Guangdong Research Center for Interfacial Engineering of Functional Materials, College of Materials Science and Engineering, Shenzhen University, Shenzhen, the People's Republic of China

Correspondence

Chunfeng Wang and Caofeng Pan, CAS Center for Excellence in Nanoscience, Beijing Key Laboratory of Micro-nano Energy and Sensor, Beijing Institute of Nanoenergy and Nanosystems, Chinese Academy of Sciences, Beijing 100049, the People's Republic of China.
Email: cfwang@szu.edu.cn and cfpan@binn.cas.cn

Abstract

The emulation of human multisensory functions to construct artificial perception systems is an intriguing challenge for developing humanoid robotics and cross-modal human–machine interfaces. Inspired by human multisensory signal generation and neuroplasticity-based signal processing, here, an artificial perceptual neuro array with visual-tactile sensing, processing, learning, and memory is demonstrated. The neuromorphic bimodal perception array compactly combines an artificial photoelectric synapse network and an integrated mechanoluminescent layer, endowing individual and synergistic plastic modulation of optical and mechanical information, including short-term memory, long-term memory, paired pulse facilitation, and "learning-experience" behavior. Sequential or superimposed visual and tactile stimuli inputs can efficiently simulate the associative learning process of "Pavlov's dog". The fusion of visual and tactile modulation enables enhanced memory of the stimulation image during the learning process. A machine-learning algorithm is coupled with an artificial neural network for pattern recognition, achieving a recognition accuracy of 70% for bimodal training, which is higher than that obtained by unimodal training. In addition, the artificial perceptual neuron has a low energy consumption of ∼20 pJ. With its mechanical compliance and simple architecture, the neuromorphic bimodal perception array has promising applications in large-scale cross-modal interactions and high-throughput intelligent perceptions.

KEYWORDS

artificial intelligent systems, mechanoluminescence, neuromorphic computing, optoelectronic synapse, visual-tactile perception

1 | INTRODUCTION

Human gather information for perception and interactions utilizing multisensory systems, which consists of diversified receptors for parallel sensing and synapse-connected neural networks for signal processing.[1–3] Significant achievements have been made in soft electronics to mimic receptors and neuromorphic electronics to mimic synapses.[4–11] For example, tactile sensors have been developed to emulate mechanoreceptors based on various working principles of piezoelectric, piezoresistive,[12] capacitive, and triboelectric,[13–17] and artificial synapses have been constructed with either two-terminal from, such as memristors, phase change memory and atomic switches, or three-terminal structures, such as ferroelectric field effect transistors, floating-gate transistors and electrolyte-gated transistors.[18–22] However, their integration to empower sensory reception remains extremely limited due to the difficulty in efficiently connecting sensors and synapses. Recently, several reception systems have been developed by integrating discrete sensing devices and synapses.[23–26] For example, Bao et al. demonstrated an artificial afferent nerve by integrating pressure sensors with a synaptic transistor utilizing the ring oscillators.[27] Chen et al. reported a tactile perceptual learning system by connecting a pressure sensor to a synaptic transistor with an ionic cable[28] and subsequently extended it to a visual-haptic perceptual system by adding photodetectors.[29] Dijken et al. developed an optoelectronic spiking afferent nerve composed of light-emitting diodes and analog-to-digital circuits and converted pressure into light pulses to modulate synaptic photomemristors.[30,31] Furthermore, Bao et al. currently demonstrated a multimodal neuromorphic electronic skin that incorporates organic semiconductor transistors, which can sense external stimuli such as temperature and pressure and encode these stimuli into electrical pulses.[32] Despite these significant advances, physically separated sensing and processing units and complex device configurations cause issues in terms of system integration, spatial resolution, data transmission latency, and energy consumption. Thus, it is highly desirable to integrate sensing, processing, learning, and memorization into one device for advanced artificial perceptual systems.

In general, optical systems have merits of concision, intuition, fast response times, and high integration.[33,34] The integration of optical receptors with optoelectronic synapses could be a promising approach to address the aforementioned issues. This method requires transduction of stimuli into lights without any auxiliary systems. Mechanoluminescence (ML) is a phenomenon that materials are capable of emitting light under mechanical stimuli and has been emerging in sensing, displays, and bioengineering.[35–40] Specifically, the force-to-light conversion of ML materials could be self-powered and self-recovered, without the assistance of electron or photon excitation, and thus holds great potential in the construction of large-scale visual-tactile perception array in a more compact, efficient, and unobtrusive fashion.

Here, we demonstrate an all-in-one bimodal perception array integrating ML materials and optoelectronic synapses for visual-tactile information sensing, processing, learning, and memorization. The optoelectronic synapses are based on an InGaZnO (IGZO) and methylammonium lead iodide (MAPbI$_3$) heterostructure, which can respond to the entire visible light spectrum in a neuromorphic manner. The tactile perception is enabled by ML materials, which convert tactile stimuli into lights that can be identified to update the weights of the optoelectronic synapses. Both visual and tactile stimulations allow short-term memory, long-term memory, paired pulse facilitation, "learning-experience", and energy-efficient synaptic behavior, enabling the implementation of the classical Pavlov's dog's conditioning experiment with spatiotemporally dynamic inputs of visual and tactile stimuli. A 6 × 6 bimodal perception array with a simple architecture is demonstrated, exhibiting an enhanced image memory utilizing synthetic visual-tactile modulation. And the device successfully realizes the recognition of handwritten digital images by simulating an artificial neural network coupled with a machine learning algorithm, performing a recognition accuracy of 70% for visual-tactile fusion, which is higher than the recognition accuracy of unimodal approaches. These functions can be further translated on flexible platforms, highlighting the viability of this technology in mechanically compliant systems.

2 | RESULTS AND DISCUSSION

2.1 | Design of the artificial visual-tactile perception array

The human perception system facilitates high-level cognition and learning with the integration and interaction of vision, hearing, touch, smell, and taste senses, among which vision accounting for more than 80% of acquired information, while touch can provide relevant information about touched objects, including force, strain, shear, flexion, torsion, and vibration. The fusion of visual and tactile sensing is a coherent and robust method for responding to stimuli, leading to extensive cross-modal plasticity in synapses for perception in cortical areas of the brain, as illustrated in Figure 1A. In parallel to human visual-tactile perception system, an artificial bimodal visual-tactile perception array integrating
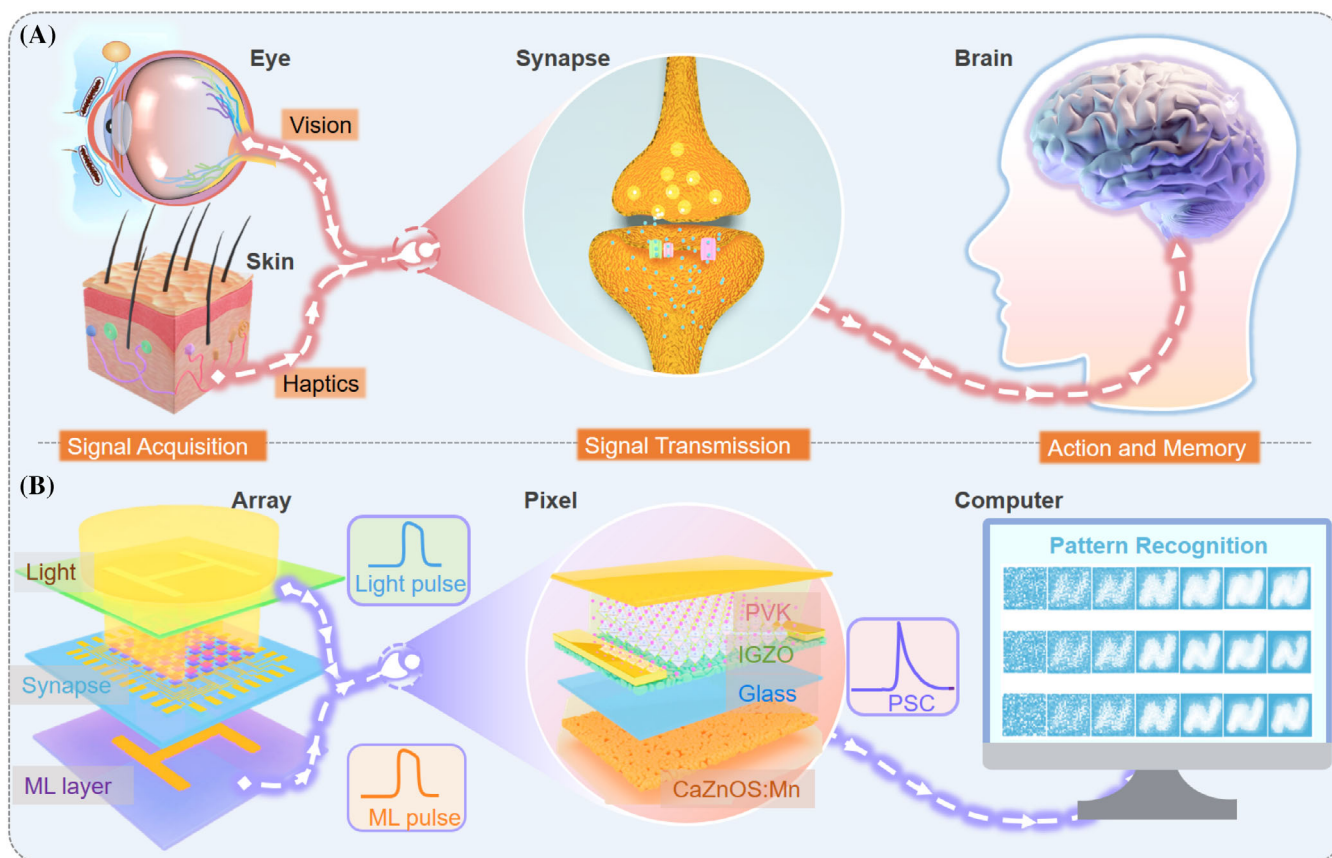
FIGURE 1 An artificial visual-tactile perception system. (A) Schematic of human visual-tactile perception system. (B) Schematic of artificial visual-tactile perception array consisting of a photoelectronic synapse network and an integrated mechanoluminescent layer.

information sensing and neuromorphic functions is proposed (see the Section 4 and Figure S1 for fabrication details). The device has a compact architecture composed of IGZO/MAPbI$_3$ heterostructure and ML layer, in which the IGZO/MAPbI$_3$ heterostructure is utilized as the base layer for both visual sensing and artificial synapse, and the ML layer enables the transduction of mechanical stimuli into lights for tactile sensing and plastic modulation of the artificial synapse. The bimodal modulation of visual and tactile stimuli realizes the enhanced processing, learning, recognition, and memorization of stimulation information, as shown in Figure 1B.

2.2 | Artificial visual perception

To mimic visual perception, the light-interactive properties of the device are first examined, as schematically shown in Figure 2A. The current variation of the device under illumination with various times, intensities, and wavelengths is depicted in Figure 2B,C, When the illumination intensity and wavelength are fixed, and the illumination time is set to 2, 4, 6, 8, and 10 s, the change in the excitatory

postsynaptic current (ΔEPSC) of the device increases continuously with the illumination time. For an illumination time of 10 s and a wavelength of 600 nm, the ΔEPSC of the device is 0.27 nA at an intensity of 1.11 μW cm^{-2}, 0.99 nA at an intensity of 5.01 μW cm^{-2}, and 1.81 nA at an intensity of 10.05 μW cm^{-2}, respectively. The device can respond well to the entire visible light range, including UV (365 nm), blue (405 nm), green (530 nm), orange (600 nm), and red (700 nm) light, at an illumination intensity of 10 μW cm^{-2}. In addition, the ΔEPSC of the device continuously increases up to 14 nA with continuous illumination (200 s, 600 nm, 1 μW cm^{-2}), then sluggishly attenuates for more than 1000 s after the illumination is removed (Figure S2), suggesting that the device displays neuromorphic light-interactive behavior, as shown in Video S1. The excellent performance is attributed to the IGZO/MAPbI$_3$ heterostructure, which not only combines the synaptic photoresponse of IGZO[41–45] (Figure S3) and the wide spectral response of MAPbI$_3$[46,47] (Figure S4), but also induces the photogate effect. As shown in Figure 2D. The electrons generated in the MAPbI$_3$ upon photoexcitation transfer to the IGZO due to the favorable energy band alignment (the decay of fluorescence lifetime of MAPbI$_3$/
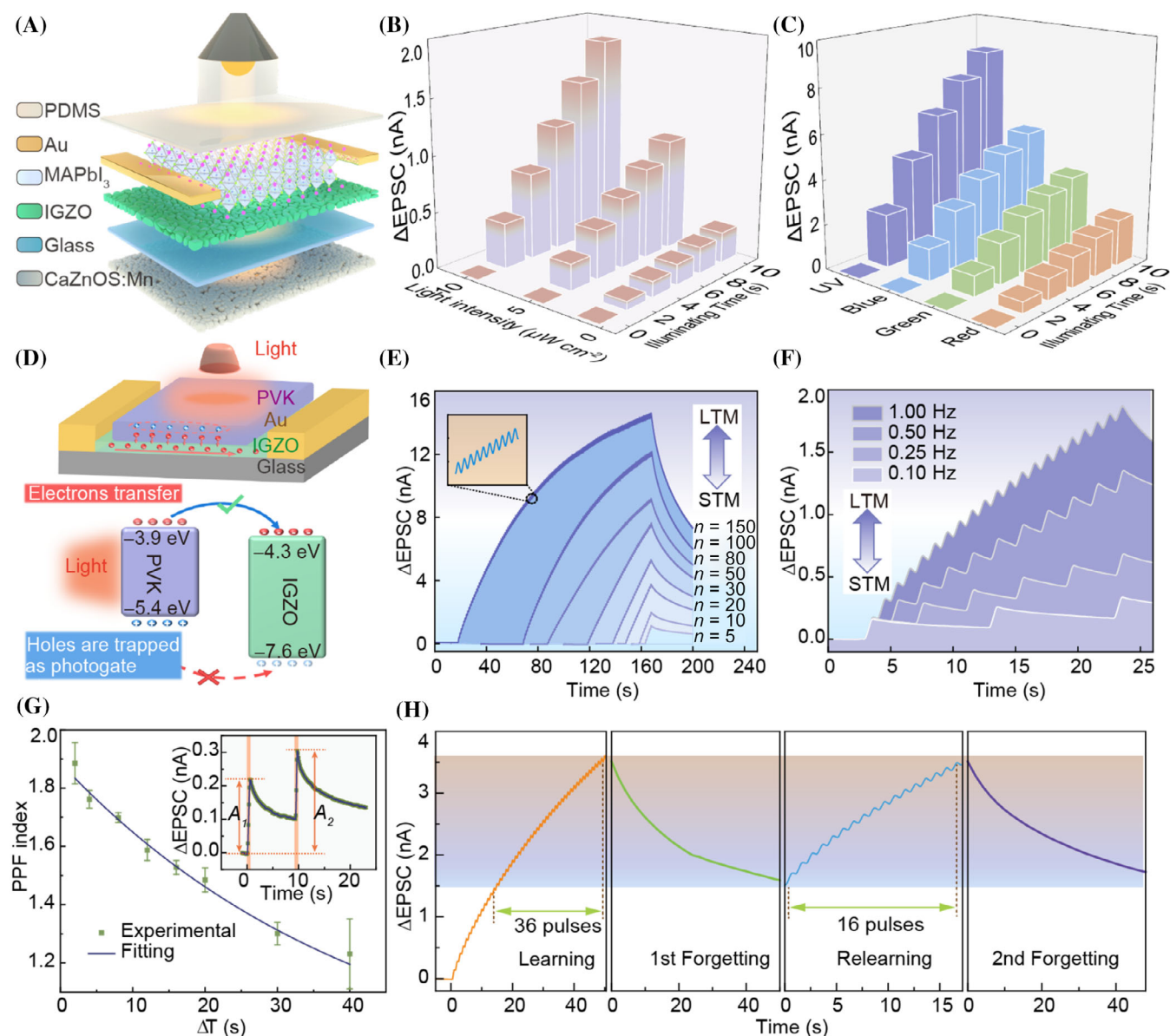
FIGURE 2 Artificial visual perception. (A) Schematic of the light-interactive device for the emulation of visual perception. (B) The current variation of the device under illumination with various time and intensity. (C) The current variation of the device under illumination with various time and wavelength. (D) Schematic diagram of the photogate effect. (E) Conversion from STM to LTM achieved by varying the number of the light pulse (wavelength = 600 nm, power density = 1 μW cm^{-2}, width = 500 ms, frequency = 1 Hz). (F) Conversion from STM to LTM achieved by varying the frequency of the light pulse (wavelength = 600 nm, power density = 1 μW cm^{-2}, width = 500 ms). (G) The variation of PPF index with the time interval of light pulse pairs. Inset: EPSC trigged by two successive light pulses with a time interval of 10 s. (H) The emulated visual learning-experience behavior of the device under pulsed light stimuli (wavelength = 600 nm, power density = 1 μW cm^{-2}, width = 500 ms, frequency = 1 Hz).

IGZO relative to MAPbI$_3$ was used as a corroboration of electron transfer, Figure S5), leaving holes trapped in the MAPbI$_3$ and a positive photogating voltage, thus enhancing the response to weak light. Moreover, the electrons entering into the IGZO were bound by oxygen vacancies in the IGZO, thus retarding the electron–hole recombination and leading to a persistent photoconductivity effect.[48,49]

The neuromorphic light-interactive behavior of the device is further characterized using light pulses (wavelength = 600 nm, power density = 1 μW cm^{-2}), similar to the spike-based information processing in the human system. The pulse signals can be integrated and converted into postsynaptic current, and the current can be modulated by varying the applied pulse width, pulse number, and pulse frequency. These characterizations

enable the emulation of short-term memory (STM), long-term memory (LTM), and the conversion of STM to LTM, which are the basis of learning and decision-making in the brain (Figure 2E,F and Figure S6). The ΔEPSC gradually changes from weak (STM) to strong (LTM) as increasing pulse number, frequency and width. In addition, the current decay time and the steady current after decay increase continuously with the increase of pulse number, frequency and width (Figure S7). Paired-pulse facilitation (PPF) describes the phenomenon that the amplitude of a postsynaptic spike evoked by a pulse increases when that pulse closely follows a prior pulse and is critical for processing temporal information in the nervous system. The device realized PPF functions with two sequential light pulses, A_1 and A_2, with a time interval of $\Delta t = 10$ s, as shown in the inset of Figure 2G. The curve of the PPF index (A_2/A_1) over the time interval fits well with the following double-phase exponential function:

$$A_2/A_1 = 1 + C_1 \times \exp(-\Delta t/\tau_1) + C_2 \times \exp(-\Delta t/\tau_2) \quad (1)$$

where C_1 and C_2 are the initial facilitation magnitudes of the respective phases, and τ_1 and τ_2 are the characteristic relaxation times of the respective phases. This result demonstrates that the device behaves similarly to a biological system (Figure 2G). The learning-experience behavior of the device was also demonstrated using two light pulse trains (Figure 2H). In the first train, the ΔEPSC of the device gradually increases from 1.5 to 3.5 nA with an excitation of 36 light pulses and then decays to an intermediate level of ∼1.5 nA within 50 s after stopping the light illumination. The behavior is analogous to the information learned by a person being partially forgotten over time. The ΔEPSC achieved by the first train can be recovered with only 16 pulses for the second train, and the ΔEPSC decay decreases within the same period of 50 s, resembling that relearning the forgotten information is easier than initially learning that information and the relearned information is significantly stronger compared to that acquired during the initial learning period.

2.3 | Artificial tactile perception

Tactile perception is demonstrated by applying a force to the ML layer, empowering the mechano-optical transduction and the sequential modulation of the synaptic plasticity, as shown in Figure 3A. The ML layer is made of ZnS-CaZnOS:Mn powders embedded in an acrylic matrix and elegantly integrated on the backside of a glass substrate (Figure S8). ZnS-CaZnOS:Mn is selected here due to its high performance in transducing forces into vivid lights with high brightness, as shown in Figure 3B and Video S2. The inset of Figure 3B shows the morphology of the ZnS-CaZnOS:Mn powders. The high brightness of ZnS-CaZnOS:Mn is ascribed to its biphase nature, consisting of a ZnS phase and a CaZnOS phase, as indicated by the x-ray diffraction (XRD) pattern and energy-dispersive x-ray spectroscopy (EDS) mapping images (Figure S9). As a result, the energy band is offset at the phase interface, improving carrier transfer and recombination.[50] Moreover, the ML layer can respond to forces as small as 2 N, and the ML intensity increases as the applied force increases, with a consistent peak wavelength of 600 nm, as shown in Figure 3C.

Similar to visual perception, the device exhibits force-induced synaptic behaviors. Such properties were emulated by the response of the device to external force pulses with different amplitudes, numbers and frequencies. As shown in Figure 3D, larger forces triggered larger postsynaptic currents, and the energy consumption of one spike can be calculated as ∼20 pJ per synaptic event according to $E = \Delta I \times V \times t$, where ΔI, V, and t represent the change in the postsynaptic current (0.05 nA at 2 N, as shown in Figure S10), the reading voltage (1 V), and the pulse duration (400 ms), respectively. The STM, LTM, and the transition of STM to LTM were realized by applying a set of force pulses (force = 5 N and duration = 400 ms) to the device, with the numbers ranging from 5 to 100 and the frequencies ranging from 0.1 to 1 Hz, as shown in Figure 3E,F, and Video S3. The PPF behavior was successfully mimicked by using two consecutive force pulses, where the ΔEPSC evoked by the second force pulse was larger than that evoked by the first pulse, with a time interval of $\Delta t = 5$ s (inset of Figure 3G). The PPF index also obeyed the double-exponential Equation (1), as shown in Figure 3G. The force-induced learning-experience behavior of the device is displayed in Figure 3H, in which 32 force pulses were first applied to the device, resulting in an increase in ΔEPSC to 1.5 nA, followed by a decay to an intermediate value of ∼0.6 nA. Only 14 force pulses were needed to recover the ΔEPSC value, and the decay lasted for a longer time than that in the first learning process.

2.4 | Visual-tactile information facilitates associative learning

Biologically, the spatiotemporally relevant inputs of spikes from multiple presynaptic neurons to a postsynaptic neuron can establish dynamic logic in a neural network. In our case, optical and force pulses were considered as presynaptic spikes and chronologically applied to the device to implement that behavior, as
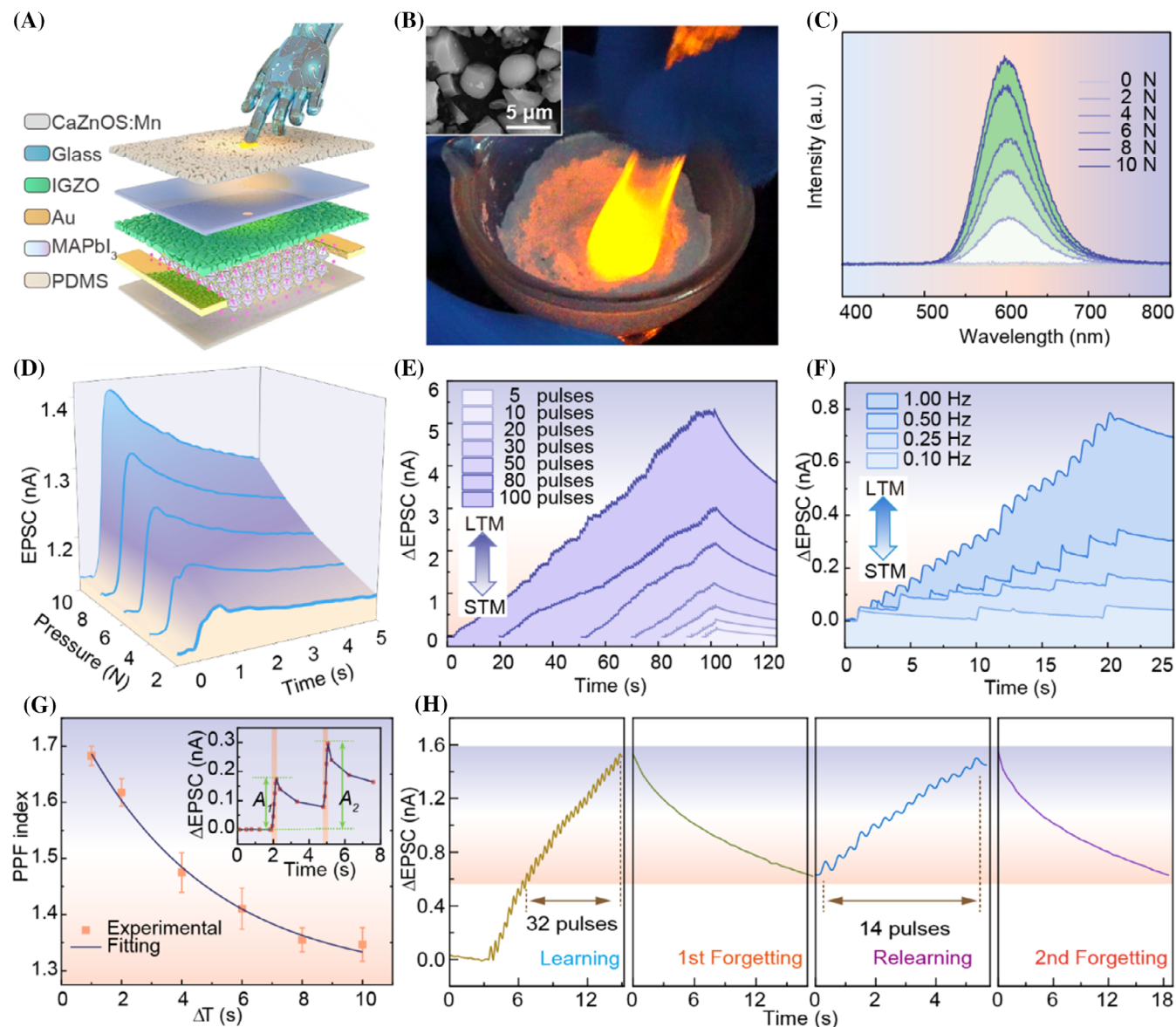
FIGURE 3 Artificial tactile perception. (A) Schematic of the force-interactive device for the emulation of tactile perception. (B) Photograph of ZnS-CaZnOS:Mn mechanoluminescent materials upon mechanical stimuli. Inset: SEM image of ZnS-CaZnOS:Mn powders. (C) The dependence of ML intensity of the ML layer made of ZnS-CaZnOS:Mn and acrylic matrix on the applied force. (D) The postsynaptic current of the device under different force magnitudes. (E) The memory behavior of the device realized by applying a set of force pulses with numbers ranging from 5 to 100 (force = 5 N, duration = 400 ms, and frequency = 1 Hz). (F) The memory behavior of the device realized by applying a set of force pulses with frequencies ranging from 0.1 to 1 Hz (force = 5 N and duration = 400 ms). (G) The PPF behavior of the device triggered by force pulses. (H) The learning-experience behavior of the device stimulated by the force pulses (force = 5 N, duration = 400 ms, and frequency = 1 Hz).

illustrated in Figure 4A and installed in Figure S11. $\Delta t_{pre2-pre1}$ is defined as the interval time between optical (presynapse2) and force (presynapse1) spikes, and the zero time is set as the starting point of applying the force spike. As shown in Figure 4B, the EPSC had a maximum value of 1.58 nA when the optical and force spikes were applied simultaneously ($\Delta t_{pre2-pre1} = 0$), which is higher than that of individual force spikes (1.23 nA) and optical spikes (1.37 nA). Moreover, the EPSC appeared to differ

when $\Delta t_{pre2-pre1} = -10$ s or 10 s, with values of 1.40 nA or 1.44 nA, corresponding to the optical spike being presented before or after the force spike, respectively. The results demonstrate that the correlation effect of two spatiotemporal-related spikes dynamically depends on $\Delta t_{pre2-pre1}$. To better reflect the spatiotemporal correlation effect of the device, the current change ratio (CCR = ΔEPSC/EPSC$_0$) as a function of $\Delta t_{pre2-pre1}$ was calculated (ΔEPSC measured at the end of the second
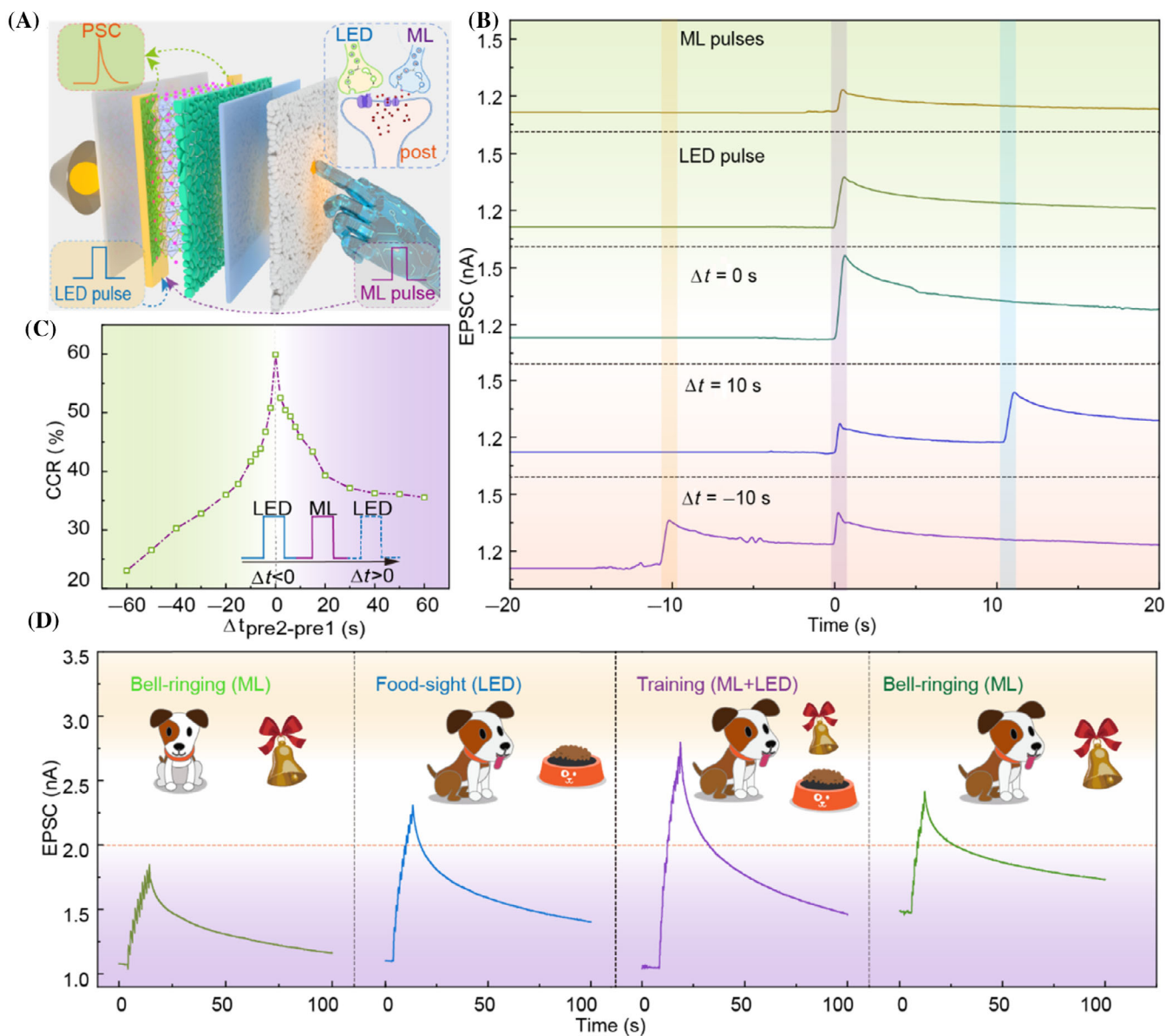
FIGURE 4 Visual-tactile facilitation for associative learning. (A) Schematic illustration of the correlation effect of the device with two spatiotemporal-related force and optical spikes. Inset shows the schematic of the biological counterparts. (B) The EPSC of the device triggered by single or superimposed force and optical spikes with spatiotemporal information. (C) The spatiotemporal correlation effect of the device plotted as a function of $\Delta t_{pre2-pre1}$. (D) Simulation of classical conditioned experiment realized by the spatiotemporally relevant inputs of force and optical spikes. (Light pulse: wavelength = 600 nm, power density = 1 μW cm^{-2}, width = 500 ms, frequency = 1 Hz; Force pulse: force = 5 N, duration = 400 ms, and frequency = 1 Hz).

stimulus). As shown in Figure 4C, the CCR significantly increases as $\left|\Delta t_{pre2-pre1}\right|$ decreases in an asymmetric manner, which is similar to the superlinear amplification behaviors of hippocampal CA_1 pyramidal neurons.[51]

The spatiotemporal correlation effect of optical and force pulses can also be used to conduct the classical conditioning experiment of Pavlov's dog, mimicking the associative learning and memory process of the human brain. The emulated training experiment is depicted in Figure 4D. Ten consecutive force pulses

(force = 5 N, duration = 400 ms, frequency = 1 Hz) were first applied to the device to emulate the bell ringing/conditional stimulus, resulting in a slight increase in the postsynaptic current (1.86 nA) that was below the threshold (2 nA) for salivation. Then, 10 consecutive optical pulses (wavelength = 600 nm, power density = 1 μW cm^{-2}, width = 500 ms, frequency = 1 Hz) were applied to the device to mimic the food sight/unconditional stimulus, resulting in a high postsynaptic current (2.33 nA) that activated

salivation. The bell ringing/conditional and food sight/unconditional stimuli were simultaneously applied to the device in the training phase, leading to a larger change in the postsynaptic current (2.80 nA) that was well above the salivation threshold. After training, a single bell ringing/conditioned stimulus could induce a postsynaptic current (2.44 nA) higher than the salivation threshold, demonstrating that an association between the bell ringing/conditional stimulus and the food sight/unconditional stimulus was established. Note that the bell ringing/conditional stimulus must be applied within 100 s after training to induce a salivation response.

2.5 | Visual-tactile perception array for enhanced image memory

Different from single-pixel devices, a device with a pixel array is capable of learning and memorizing images. In this context, a visual-tactile perception array with 6×6 units was constructed, and the operating schematic diagram is shown in Figure 5A. A photomask was used to apply the patterned optical stimulus to the top of the device, while the mechanical stimulus pattern was applied to the device through the bottom ML layer. The lower-right inset of Figure 5A shows a photograph of the array device, and the lower-left inset represents the ML pattern, which can easily be adjusted (Figure S12). The responses of a representative perception pixel to individual or superimposed inputs of optical (pulse number = 10, wavelength = 600 nm, power density = 1 μW cm^{-2}, width = 500 ms, frequency = 1 Hz) and mechanical (pulse number = 10, force = 5 N, duration = 400 ms, frequency = 1 Hz) stimuli are shown in Figure 5B. The results show that the synergetic light and force stimuli lead to a postsynaptic current of 3.17 nA, which is approximately the sum of the individual current generated by the optical or mechanical stimuli. The combined optical and mechanical stimuli enable the current to be maintained longer than that when the individual stimuli are applied, indicating the enhanced memory (Figure 5C). The image memorization function of the array device for light and force distributions is demonstrated in Figure 5D. The letter of "H" can easily be recognized after stimulation by the light pattern, force pattern, or a combination of the two. Nevertheless, the images gradually became incomplete at a time of 30 or 60 s after separate force or light stimuli were applied, respectively, but could still be identified after 100 s when the integrated stimuli were used, indicating that the memorization effect of the device was significantly enhanced by the combined stimuli.

2.6 | Flexible visual-tactile perception array for enhanced neuromorphic computing

The visual-tactile perception array was also fabricated on a flexible substrate to enable its integration in mechanically compliant systems. Figure 6A shows a photograph of the flexible device with a PET substrate. The flexile device can be bent to different radii of curvature of 5, 10, and 15 mm, while the deviation in EPSC is less than 10% (Figure 6B), demonstrating the good mechanical compliance of the device. In addition, the performance of the flexible device did not degrade significantly after 500 bending cycles at a radius of curvature of 10 mm, as shown in Figure 6C, indicating the good mechanical robustness of the device.

An artificial neural network (ANN) was simulated using the flexible visual-tactile perception array, in order to perform supervised learning with Modified National Institute of Standards and Technology (MNIST) handwritten images. As shown in Figure 6D and Figure S13, the designed ANN is composed of an input layer, an output layer, and a synaptic connection layer. Each layer consists of 785 input neurons (i.e., 1 bias neuron and 28×28 neurons), 10 output neurons (from 0 to 9), and $785 \times 10 = 7850$ synapses, respectively. The simulation process of ANN is divided into a feedforward process and a back-propagation process. In the feedforward process, the training picture is divided into 28 by 28 pixels, and each of them is converted into a voltage vector (V), which is multiplied by the weight matrix (W) of the synapse array to obtain the current vector (I). The current vector is then transformed to the output vector (y) through a sigmoid activation function, $y = f(I)$. There will be a deviation between the output vector and the label value (k) of the input image. The deviation value is calculated and backpropagated to the synapse layer with a hardware-based backpropagation algorithm to guide the weight update process, which is executed by applying the corresponding number of light/force pulses. We use the change in the conductivity of the device to simulate the weight update process of the neural network, and $G_{\max}/G_{\min}$ plays a crucial role in the weight update process and ultimately affects the recognition rate (see Section 4 for the details of the weight update method). With this approach, we successfully completed the recognition of 26 letters from "A" to "Z" by expanding the number of MNIST training datasets (188958) and test datasets (31346). As a representative example, the recognition process of the letter "N" is shown in Figure 6E, where the synaptic weights were updated in three cases—force, light, and a combination of the two. A clearer image was obtained by applying mixed light and
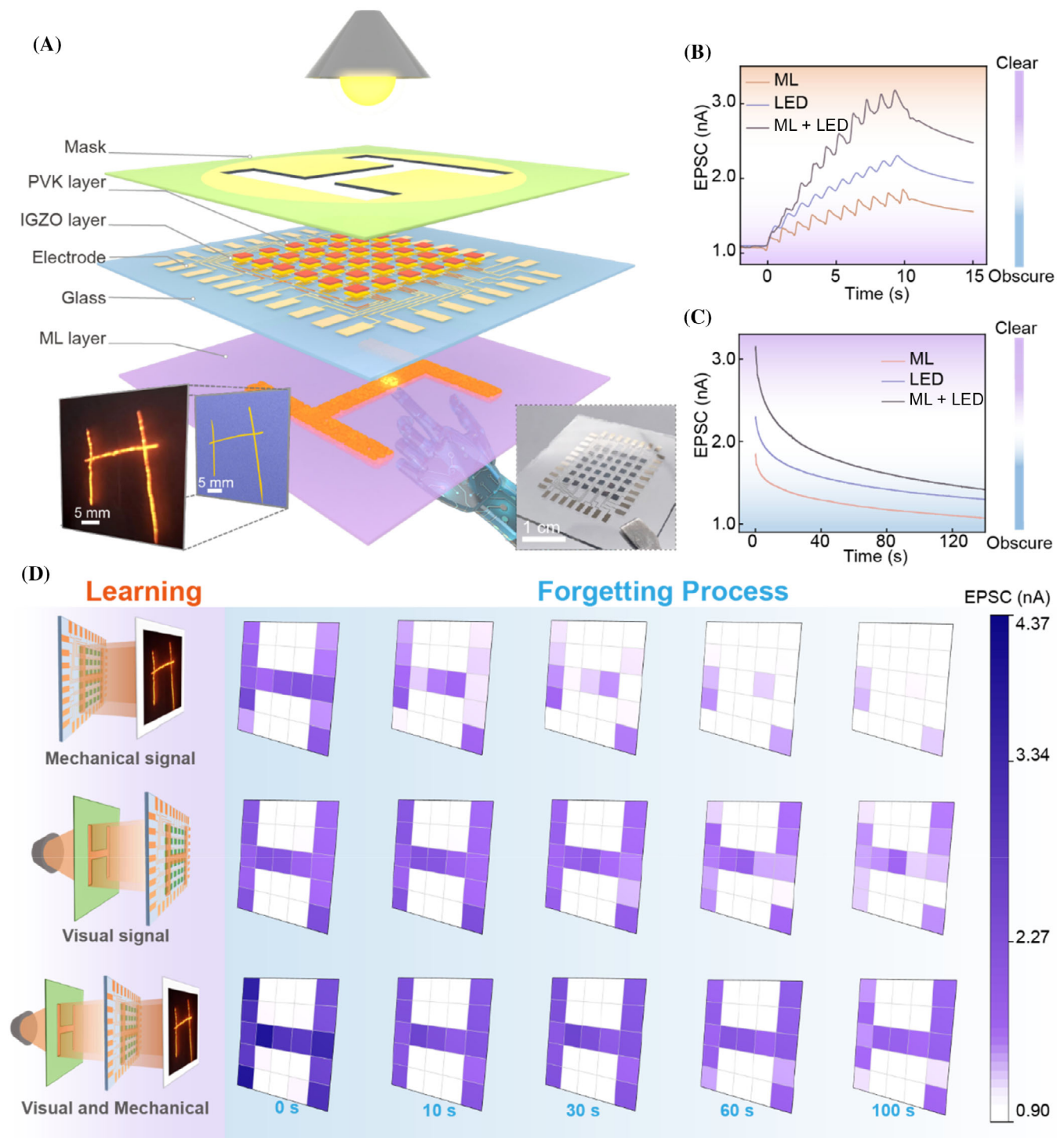
FIGURE 5 Visual-tactile perception array for enhanced image memory. (A) Schematic of the visual-tactile perception array device under the light and force stimulus. Inset shows the photograph of the device. (B) The response of a representative perception pixel to the individual or superimposed inputs of light and force stimulus. (C) The decay of the postsynaptic current generated by the individual or superimposed inputs of light and force stimulus. (D) The image memorizing function of the array device for light and force distribution. (Light pulse: wavelength = 600 nm, power density = 1 µW cm^{-2}, width = 500 ms, frequency = 1 Hz; Force pulse: force = 5 N, duration = 400 ms, and frequency = 1 Hz).

force pulses, demonstrating the enhanced neuromorphic computing capability of the proposed approach. The enhancement is enabled by the bimodal neuroplastic modulation induced by the light and force pulses, leading to a larger change in the conductivity. Figure 6F shows the change in the conductivity as a function of the
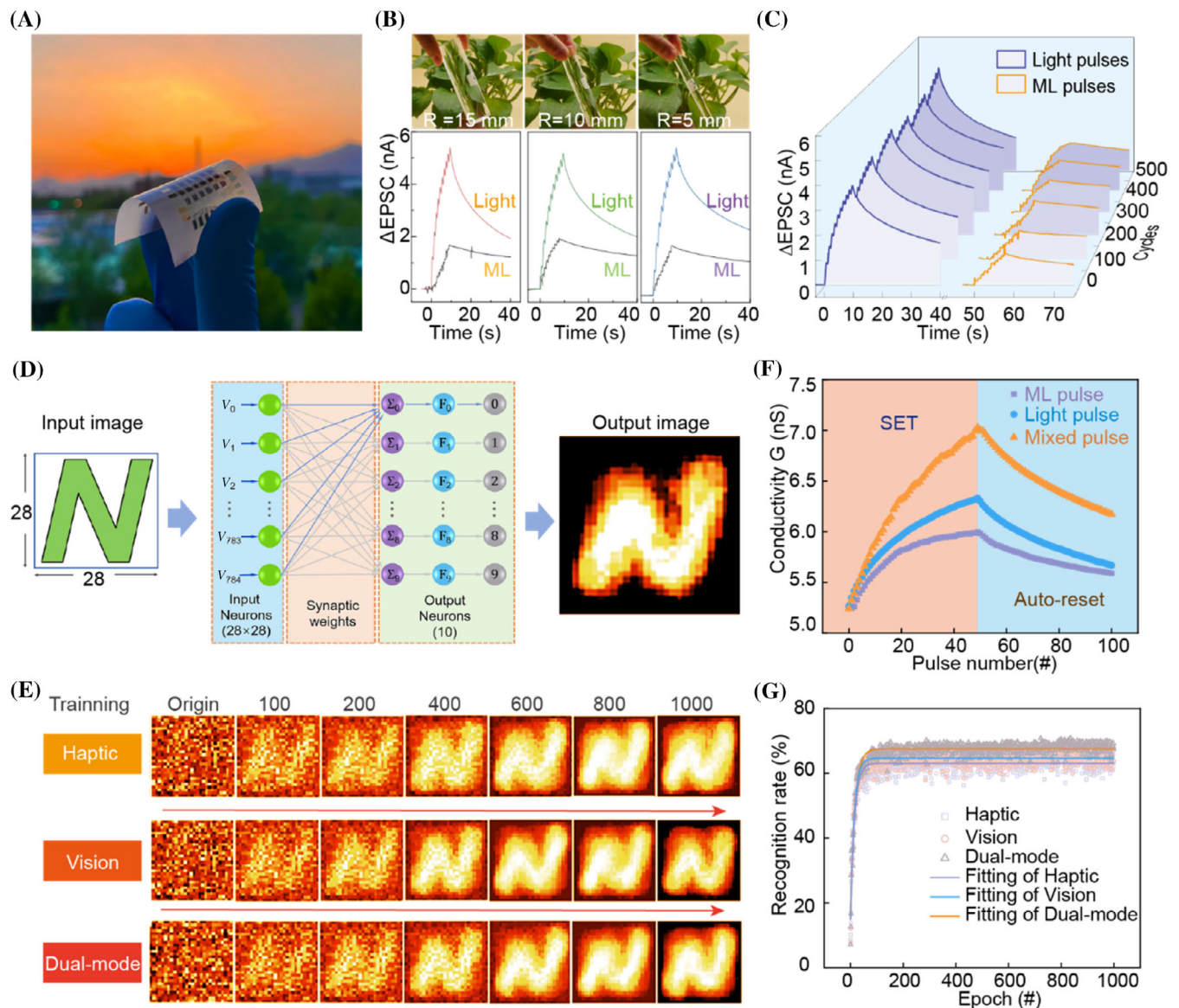
FIGURE 6 Flexible visual-tactile perception array for enhanced neuromorphic computing. (A) Photography of the flexible visual-tactile perception array. (B) The ΔEPSC of the flexible device tested on glass rod surfaces of different radii of curvature (15, 10, and 5 mm) with stimulations of 10 light pulses and 10 force pulses, respectively. (C) The ΔEPSC of the flexible device stimulated by 10 light pulses and 10 force pulses during 500 bending cycles at a radius of curvature of 15 mm. (D) Schematic of ANN architecture. (E) The pattern recognition of "N" with the evolution of training epochs. (F) The change in the conductivity as function of the number of applied light, force, and light-force pulses, respectively. (G) The recognition rates of ANN as a function of the training epoch number, modulated by the force, light, or a combination of them. (Light pulse: wavelength = 600 nm, power density = 1 μW cm^{-2}, width = 500 ms, frequency = 1 Hz; force pulse: force = 5 N, duration = 400 ms, and frequency = 1 Hz).

number of applied light, force, and light-force pulses, showing that G_{max}/G_{min} in the potentiation phase increased more significantly when the mixed spikes were applied than when the individual spikes were applied. And the recognition rates of the ANN as functions of the training epoch number were calculated and are shown in Figure 6G to clarify the enhancement in a quantitative manner. The recognition rates in the case of light and force fusion exhibited a high saturated recognition rate of

~70%, which is higher than that of individual light pulses (~65%) or force pulses (~61%).

3 | CONCLUSION

In summary, for the first time, ML materials were combined with an optoelectronic synapse network based on IGZO/MAPbI$_3$ heterostructure to integrate sensing,

memory, and neuromorphic computing functions into one flexible artificial visual-tactile perception array in a simple, highly efficient, compact, and large-scale manner, which may mitigate the integration and power consumption issues observed in multisensory perception systems. The artificial visual-tactile perception array exhibits key features of receptors and synapses in response to optical and mechanical stimuli, endowing the individual or synergistic sensing and plastic modulation of optical and mechanical information. The device not only simulates an associative learning process with spatiotemporally dynamic inputs of light and force stimuli, but also enhances the memory and recognition accuracy of the image information utilizing mixed pulses of light and force. This work provides a new paradigm for the development of multifunctional and highly compact neuromorphic devices with a wide range of potential applications, such as humanoid robotics and cyborg systems.

4 | EXPERIMENTAL SECTION

4.1 | Materials

ZnS (99.99%, Aladdin), $MnCO_3$ (>99.99%, Sigma-Aldrich), eggshell powders, CH_3NH_3I (≥99.99, Xi'an Polymer Light Technology Corp), PbI (≥99.99, Xi'an Polymer Light Technology Corp), N,N-dimethylformamide (DMF 99.5%, Aladdin) and dimethyl sulfoxide (>99%, Aladdin), PDMS matrix (Sylgard 184, Dow Corning), and epoxy resin were all purchased and used as received.

4.2 | Synthesis of ML materials

The ML material of ZnS–CaZnOS:Mn was prepared via a conventional high-temperature solid-state reaction, as reported in our previous work.[34] Briefly, the eggshell powder was mixed with ZnS powder and $MnCO_3$ powder in the molar ratio of Ca:Zn:Mn = 1:2:0.01, where the content of $CaCO_3$ in the eggshell powder was estimated to be 90% by weight. The mixture was mixed in a ball mill for 30 min with the help of anhydrous ethanol, and then dried in a desiccator at 80°C for 4 h. The dried mixture was transferred into a corundum crucible and calcined in a furnace at 1100°C for 4 h under 80 sccm Ar gas. After natural cooling of the furnace to room temperature, the product was ground and sieved to obtain relatively uniform particle size particles for use. The ML materials have a light-emitting wavelength overlapping well with that of the light-emitting diode used for the visual synaptic modulation, as shown in Figure S14.

4.3 | Fabrication of artificial visual-tactile perception array device

The fabrication process of visual-tactile perception device is schematically shown in Figure S1. A transparent substrate (glass or PET) was ultrasonically cleaned in acetone, isopropyl alcohol, and deionized water, respectively, and then dried with nitrogen gas. After treatment with oxygen plasma for 5 min, the gold electrodes with a channel width of 100 μm and a thickness of 30 nm were deposited on the substrate by a combination of lithography and DC magnetron sputtering (PVD75 Kurt J. Lesker, Ar, 4 mTorr, 80 W, 3 min). Sequentially, a heterogeneous layer composed of 80 nm thick amorphous IGZO and 200 nm $MAPbI_3$ was deposited on the electrode utilizing sputtering and spin-coating, respectively (The microscopic morphological characterisations are shown in Figure S15). The IGZO layer was manufactured by RF magnetron sputtering (PVD75 Kurt J. Lesker, Ar, 4 mTorr, 80 W, 30 min). The precursor for $MAPbI_3$ is a mixture of CH_3NH_3I and PbI_2 with a molar ratio of 1:1, which was dissolved in a solution containing of dimethyl sulfoxide and N,N-dimethylformamide with a volume ratio of 1:4. The spin-coating process was proceed in a glove box at 5000 rpm for 60 s, during which chlorobenzene was used as an anti-solvent and added dropwise at the 10th second. The $MAPbI_3$ film was packaged with a thin layer of polydimethylsiloxane (PDMS) to improve the device stability. At last, a ML layer consisting of ZnS–CaZnOS:Mn and epoxy resin with a weight ratio of 7:3 was spin-coated (1000 rpm for 60 s) on the other side of the substrate, followed by a desiccation at 80°C for 4 h.

4.4 | Characterizations

The morphology and composition were characterized using a scanning electron microscope (SEM, FEI Nova NanoSEM 450) equipped with EDAX (EDS). XRD patterns were obtained using an x-ray diffractometer (PANalytical X'Pert 3 Powder) with a Cu Kα radiation source. The surface roughness was measured by AFM (Asylum Research MFP-3D-SA). The absorption spectra were detected by Shimadzu UV 3600. The transient decay curves were obtained using an Edinburgh FLS1000 spectrometer. The mechanoluminescent spectra were characterized by a homemade measurement system consisting of a linear motor, a fiber optic spectrometer (Ocean QE65 Pro), and a dynamometer. The electrical properties of the device were measured with a Keithley 4200 SCS, Stanford DS345, and SR570 (Stanford Research Systems). The reading voltage keeps at 1 V for all measurements. All continuous light and pulsed light stimulation were

achieved by an arbitrary/functional generator (Tektronix AFG3011C) to drive the corresponding light emitting diodes. The continuous force and pulsed force stimulation were applied by a combined linear motor and dynamometer unit (The test setup diagram is shown in Figure S11).

4.5 | Weight updating method of ANN

The measured conductance values of the devices are only positive, so two devices are needed to represent a unit synapse. This is because the synaptic weights of unit synapses in ANN ($W_{i,j}$ are the synaptic weights between the i-th neuron in the input layer and the j-th neuron in the output layer) should have positive and negative values for learning. Thus, the synaptic weight ($W = G^+ - G^-$) is represented by the difference between the conductance values of the two devices (G^+ and G^-). After obtaining ΔW, the sign of ΔW determines whether the synaptic weight should be potentiated or depressed.

$$\Delta W > 0 \text{ if } k - y > 0 \text{ (potentiation)} \tag{2}$$

$$\Delta W < 0 \text{ if } k - y < 0 \text{ (depression)} \tag{3}$$

As shown in Equations (2) and (3), for the potentiation phase ($\Delta W > 0$), G^+ should increase and G^- should remain the same ($W\uparrow = G^+\uparrow - G, \ \Delta W = \Delta G^+$). Conversely, for the depression phase ($\Delta W < 0$), G^+ should remain the same and G^- should increase simultaneously ($W\downarrow = G^+ - G^-\uparrow, \ \Delta W = -\Delta G^-$). The amount of conductance change (ΔG) of G^+ and G^- can be determined as follows.

$$G_{n+1} = G_n + \Delta G = G_n + \alpha e^{-\beta \frac{G_n - G_{\min}}{G_{\max} - G_{\min}}} \ (\text{for } G^+ \uparrow \text{ or } G^- \uparrow) \tag{4}$$

$$G_{n+1} = G_n + \Delta G = G_n - \alpha e^{-\beta \frac{G_{\max} - G_n}{G_{\max} - G_{\min}}} \ (\text{for } G^+ \downarrow \text{ or } G^- \downarrow) \tag{5}$$

Here, G_n and G_{n+1} denote the value of the current conductivity state and the updated value, respectively. The parameters α and β indicate the step size and nonlinear (NL) value of conductivity change, respectively. In addition, $G_{\max}$ and $G_{\min}$ are the maximum and minimum conductivity of the device, respectively. When G^+ and G^- reach $G_{\max}$, they are initialized to $G_{\min}$. The above procedure is implemented using MATLAB, where the specific values obtained by our device are shown in Table S1.

CONFLICT OF INTEREST STATEMENT
The authors declare no conflict of interest.

ORCID
Caofeng Pan https://orcid.org/0000-0001-6327-9692

REFERENCES

1. Kim S, Roe DG, Choi YY, et al. Artificial stimulus-response system capable of conscious response. *Sci Adv.* 2021;7(15): eabe3996.
2. Jung YH, Park B, Kim JU, Kim TI. Bioinspired electronics for artificial sensory systems. *Adv Mater.* 2019;31(34): 1803637.
3. Sun FQ, Lu QF, Hao MM, et al. An artificial neuromorphic somatosensory system with spatio-temporal tactile perception and feedback functions. *npj Flexible Electron.* 2022;6(1):72.
4. Wei HH, Shi RC, Sun L, et al. Mimicking efferent nerves using a graphdiyne-based artificial synapse with multiple ion diffusion dynamics. *Nat Commun.* 2021;12(1):1068.
5. Kim J, Song S, Lee JM, et al. Metal-oxide heterojunction optoelectronic synapse and multilevel memory devices enabled by broad spectral photocarrier modulation. *Small.* 2023;35:2301186.
6. Chen S, Zhang T, Tappertzhofen S, Yang Y, Valov I. Electrochemical memristor-based artificial neurons and synapses—fundamentals, applications, and challenges. *Adv Mater.* 2023; 35(37):e2301924.
7. Baek JH, Kwak KJ, Kim SJ, et al. Two-terminal lithium-mediated artificial synapses with enhanced weight modulation for feasible hardware neural networks. *Nano-Micro Lett.* 2023; 15(1):69.
8. Jiang Z, Chen N, Yi ZG, et al. A 1.3-micrometre-thick elastic conductor for seamless on-skin and implantable sensors. *Nat Electron.* 2022;5(11):784-793.
9. Oh S, Cho JI, Lee BH, et al. Flexible artificial Si-In-Zn-O/ion gel synapse and its application to sensory-neuromorphic system for sign language translation. *Sci Adv.* 2021;7(44):eabg9450.
10. Zhu QB, Li B, Yang DD, et al. A flexible ultrasensitive optoelectronic sensor array for neuromorphic vision systems. *Nat Commun.* 2021;12(1):1798.
11. Han X, Xu ZS, Wu WQ, et al. Recent progress in optoelectronic synapses for artificial visual-perception system. *Small Struct.* 2020;1(3):2000029.

12. Wen XN, Wu WZ, Pan CF, et al. Development and progress in piezotronics. *Nano Energy*. 2015;14:276-295.

13. Chun S, Kim JS, Yoo Y, et al. An artificial neural tactile sensing system. *Nat Electron*. 2021;4(6):429-438.

14. Wang CF, Dong L, Peng DF, et al. Tactile sensors for advanced intelligent systems. *Adv Intell Sys*. 2019;1(8): 1900090.

15. Wang M, Luo YF, Wang T, et al. Artificial skin perception. *Adv Mater*. 2021;33(19):2003014.

16. Zhang JH, Yao HM, Mo JY, et al. Finger-inspired rigid-soft hybrid tactile sensor with superior sensitivity at high frequency. *Nat Commun*. 2022;13(1):5076.

17. Liu JH, Zhang ZC, Qiao S, et al. Lateral bipolar photoresistance effect in the CIGS heterojunction and its application in position sensitive detector and memory device. *Sci Bull*. 2020;65(6): 477-485.

18. Jia MM, Guo PW, Wang W, et al. Tactile tribotronic reconfigurable p-n junctions for artificial synapses. *Sci Bull*. 2022;67(8):803-812.

19. Liu QH, Yin L, Zhao C, et al. All-in-one metal-oxide heterojunction artificial synapses for visual sensory and neuromorphic computing systems. *Nano Energy*. 2022;97:107171.

20. Sarkar T, Lieberth K, Pavlou A, et al. An organic artificial spiking neuron for in situ neuromorphic sensing and biointerfacing. *Nat Electron*. 2022;5(11):774-783.

21. Sarwat SG, Kersting B, Moraitis T, Jonnalagadda VP, Sebastian A. Phase-change memtransistive synapses for mixed-plasticity neural computations. *Nat Nanotechnol*. 2022;17(5):507-513.

22. Shi JL, Jie JS, Deng W, et al. A fully solution-printed photosynaptic transistor array with ultralow energy consumption for artificial-vision neural networks. *Adv Mater*. 2022; 34(18):2200380.

23. Liu L, Xu WL, Ni Y, et al. Stretchable neuromorphic transistor that combines multisensing and information processing for epidermal gesture recognition. *ACS Nano*. 2022;16(2):2282-2291.

24. Wan HC, Zhao JY, Lo LW, et al. Multimodal artificial neurological sensory-memory system based on flexible carbon nanotube synaptic transistor. *ACS Nano*. 2021;15(9):14587-14597.

25. Yu JR, Gao GY, Huang JR, et al. Contact-electrification-activated artificial afferents at femtojoule energy. *Nat Commun*. 2021;12(1):1581.

26. Yu JR, Yang XX, Gao GY, et al. Bioinspired mechano-photonic artificial synapse based on graphene/MoS$_2$ heterostructure. *Sci Adv*. 2021;7(12):eabd9117.

27. Kim Y, Chortos A, Xu WT, et al. A bioinspired flexible organic artificial afferent nerve. *Science*. 2018;360(6392):998-1003.

28. Wan CJ, Chen G, Fu YM, et al. An artificial sensory neuron with tactile perceptual learning. *Adv Mater*. 2018;30(30): 1801291.

29. Wan CJ, Cai PQ, Guo XT, et al. An artificial sensory neuron with visual-haptic fusion. *Nat Commun*. 2020;11(1):4602.

30. Tan HW, Tao QZ, Pande I, et al. Tactile sensory coding and learning with bio-inspired optoelectronic spiking afferent nerves. *Nat Commun*. 2020;11(1):1369.

31. Tan HW, Zhou YF, Tao QZ, et al. Bioinspired multisensory neural network with crossmodal integration and recognition. *Nat Commun*. 2021;12(1):1120.

32. Wang W, Jiang Y, Zhong D, et al. Neuromorphic sensorimotor loop embodied by monolithically integrated, low-voltage, soft e-skin. *Science*. 2023;380(6646): 735-742.

33. Yu RJ, Zhang XH, Gao CS, et al. Low-voltage solution-processed artificial optoelectronic hybrid-integrated neuron based on 2D MXene for multi-task spiking neural network. *Nano Energy*. 2022;99:107418.

34. Zhu Y, Wu C, Xu Z, et al. Light-emitting memristors for optoelectronic artificial efferent nerve. *Nano Lett*. 2021;21(14):6087-6094.

35. Hou B, Yi LY, Li C, et al. An interactive mouthguard based on mechanoluminescence-powered optical fibre sensors for bite-controlled device operation. *Nat Electron*. 2022;5(10): 682-693.

36. Ma X, Wang C, Wei R, et al. Bimodal tactile sensor without signal fusion for user-interactive applications. *ACS Nano*. 2022; 16(2):2789-2797.

37. Wang CF, Ma RH, Peng DF, et al. Mechanoluminescent hybrids from a natural resource for energy-related applications. *InfoMat*. 2021;3(11):1272-1284.

38. Wei RL, He JQ, Ge SP, et al. Self-powered all-optical tactile sensing platform for user-interactive interface. *Adv Mater Technol*. 2023;8(1):202200757.

39. Yang F, Wu X, Cui H, et al. Palette of rechargeable mechanoluminescent fluids produced by a biomineral-inspired suppressed dissolution approach. *J Am Chem Soc*. 2022;144(40):18406-18418.

40. Zhuang YX, Xie RJ. Mechanoluminescence rebrightening the prospects of stress sensing: A review. *Adv Mater*. 2021;33(50): 2005925.

41. Noh H-K, Chang KJ, Ryu B, Lee WJ. Electronic structure of oxygen-vacancy defects in amorphous In-Ga-Zn-O semiconductors. *Phys Rev B*. 2011;84(11):115205.

42. Lee M, Lee W, Choi S, et al. Brain-inspired photonic neuromorphic devices using photodynamic amorphous oxide semiconductors and their persistent photoconductivity. *Adv Mater*. 2017;29(28):1700951.

43. Kwon SM, Cho SW, Kim M, Heo JS, Kim YH, Park SK. Environment-adaptable artificial visual perception behaviors using a light-adjustable optoelectronic neuromorphic device array. *Adv Mater*. 2019;31(52):1906433.

44. Kim M-K, Lee J-S. Synergistic improvement of long-term plasticity in photonic synapses using ferroelectric polarization in hafnia-based oxide-semiconductor transistors. *Adv Mater*. 2020; 32(12):1907826.

45. Abbott LF, Regehr WG. Synaptic computation. *Nature*. 2004; 431(7010):796-803.

46. Wu W, Wang X, Han X, et al. Flexible photodetector arrays based on patterned CH$_3$NH$_3$PbI$_{3-x}$Cl$_x$ perovskite film for real-time photosensing and imaging. *Adv Mater*. 2019;31(3): 1805913.

47. Dou L, Yang Y, You J, et al. Solution-processed hybrid perovskite photodetectors with high detectivity. *Nat Commun*. 2014; 5(1):5404.

48. Sun ZH, Li JH, Liu CM, et al. Trap-assisted charge storage in titania nanocrystals toward optoelectronic nonvolatile memory. *Nano Lett*. 2021;21(1):723-730.

49. Wei SL, Wang F, Zou XM, et al. Flexible quasi-2D perovskite/IGZO phototransistors for ultrasensitive and broadband photodetection. *Adv Mater.* 2020;32(6):1907527.

50. Peng DF, Jiang Y, Huang BL, et al. A ZnS/CaZnOS heterojunction for efficient mechanical-to-optical energy conversion by conduction band offset. *Adv Mater.* 2020;32(16): 1907747.

51. Yoneyama M, Fukushima Y, Tsukada M, Aihara T. Spatiotemporal characteristics of synaptic EPSP summation on the dendritic trees of hippocampal CA_1 pyramidal neurons as revealed by laser uncaging stimulation. *Cogn Neurodyn.* 2011; 5(4):333-342.

SUPPORTING INFORMATION

Additional supporting information can be found online in the Supporting Information section at the end of this article.